Full length article

Patterned nano-domains in PMN-PT single crystals

Wei-Yi Chang [a], Ching-Chang Chung [b], Zhongyuan Yuan [a], Chih-Hao Chang [a], Jian Tian [c], Dwight Viehland [d], Jie-Fang Li [d], Jacob L. Jones [b], Xiaoning Jiang [a, *]

[a] Department of Mechanical and Aerospace Engineering, North Carolina State University, Raleigh, NC 27695, United States
[b] Department of Materials Science and Engineering, North Carolina State University, Raleigh, NC 27695, United States
[c] CTS Corporation, 479 Quadrangle Dr., Bolingbrook, IL 60400, United States
[d] Department of Materials Science and Engineering, Virginia Tech, Blacksburg, VA 24061, United States

ARTICLE INFO

ABSTRACT

The domain structure, dielectric, and piezoelectric properties of 0.7 Pb(Mg$_{1/3}$Nb$_{2/3}$)O$_3$-0.3PbTiO$_3$ (PMN-PT) single crystals with nanocomposite electrode, which includes MnO$_x$ semiconductor nanogratings and a Ti/Au conductive layer, were studied in this paper. These artificial MnO$_x$ nanogratings can alter the electric field distribution and then enhance the domain density. PMN-PT crystals with Ti/Au-MnO$_x$ nanocomposite electrodes showed high piezoelectric constant of 2250 p.m./V and dielectric constant of 5400 at 1 kHz, respectively. Compared to ones with conventional planar electrodes, the piezoelectric and dielectric constants of the samples with nanocomposite electrodes were increased 36.7% and 38.3%, respectively. Piezoresponse force microscopy (PFM) images revealed the domain pattern near the electrode/single crystal interface. A linear domain structure induced by the MnO$_x$ nanocomposite electrode was found in the samples with thickness less than 200 μm. Time-of-flight secondary ion mass spectrometry (TOF-SIMS) results showed the diffusion of Mn about 300 nm in depth in PMNPT crystal after heat treatment during MnO$_x$ nanocomposite electrode. It is believed that the localized high electric fields induced by fringe effects caused by the nanocomposite electrode can enhance nucleation of new domains, and that diffusion from the patterned Mn layer may also lead to an enhancement in domain wall mobility. Our findings open up a new domain engineering technique for tailoring the dielectric and piezoelectric properties of PMN-PT single crystals.

© 2017 Acta Materialia Inc. Published by Elsevier Ltd. All rights reserved.

1. Introduction

Relaxor ferroelectric single crystals have been widely used in electro-active devices due to their excellent piezoelectric and dielectric properties near the morphotropic phase boundary (MPB) [1,2]. It is widely accepted that the enhanced piezoelectric response and poling efficiency near the MPB are due to an increased number of allowable domain states [3–6]. Moreover, the piezoelectric and dielectric properties of a ferroelectric material are highly related to its domain wall features [7]. Thus, the piezoelectric properties of ferroelectric materials can be tailored by domain engineering techniques [8,9]. The most commonly used domain engineering technique is the manipulation of the domain wall mobility by adding acceptor or donor type dopants [10].

In recent years, it was also reported that domain engineering can be achieved by using micro-patterned metal electrodes. Uneven electric fields could form in a single crystal with patterned electrodes during electrical poling, which can be used for tailoring the domain structure and piezoelectric properties of ferroelectrics [11–13] [14,15]. Wada et al. reported that the domain size in BaTiO$_3$ single crystal could be effectively reduced by using a patterned electrode during the electrical poling process. The domain size of BaTiO$_3$ with a planar electrode was larger than 5 μm, and the domain size of BaTiO$_3$ with a patterned electrode was smaller than 3 μm [16]. The piezoelectric coefficient (d$_{31}$) of BaTiO$_3$ with smaller domain sizes (i.e., patterned electrodes) was found to be −243.2 pC/N, which is significantly higher in absolute amplitude than −62.0 pC/N of the ones with larger domain sizes (i.e., planar electrodes) [16]. The enhanced piezoelectric coefficient in the BaTiO$_3$ with a patterned electrode has evidenced that the patterned

electrode method is a powerful technique for manipulating the properties of ferroelectrics.

The dielectric and piezoelectric properties of PMN-PT have been studied using metal-based electrodes for several years [2,17]. Recently, a composite electrode method including conductive and semi-conductive layer on the ferroelectric relaxors has been developed for better piezoelectric properties [18]. Mn oxides (MnO_x) are considered to be the suitable semiconductor materials for the semi-conductive layer since the electrical resistivity is ranging from 1 to 10^5 Ωcm [19]. Yamashita et al. used a sol-gel method to coat a high density, but randomly distributed MnO_x patterns, on PMN-PT single crystals as a part of the composite electrode. PMN-PT with a composite electrode exhibited nearly a 40% improvement in their longitudinal piezoelectric (d_{33}) values [18]. The authors attributed the enhanced d_{33} values to the effects of the composite electrodes on the domain structure. Similar behavior was also observed in a PMN-PT single crystal with a periodical nanocomposite electrode, which exhibits an enhanced piezoelectric properties[24]. The composite electrode may prevent rapid domain reversal when electric fields are applied to the PMN-PT crystal, as the electrical flux in the sample is nonuniform [18]. Furthermore, more new domains may nucleate at the interfaces between patterned composite electrodes and single crystal due to surface doping effect [20]. Based upon Landauer's nucleation theory, the nucleation of new domains is the initial stage of domain evolution during polarization reversal [21]. Formation of smaller domains is the key approach for enhancing piezoelectric properties [22], which is usually defect-assisted [23]. Surface doping effect has been observed in the lithium tantalite substrate with a periodic nickel grating [24]. The diffused ions could enhance the domain nucleation probability and enhance domain wall motion [25]. A powerful tool to quantify oxide ion diffusion and evaluate diffusion depth profile is time-of-flight secondary ion mass spectrometry (ToF-SIMS) [26,27]. The existing known fact is an enhancement in the piezoelectric properties with a micro/nano-patterned composite electrode can be achieved in ferroelectric single crystals [18,28]. However, the influence of the MnO_x nanocomposite electrode on the mechanisms of domain formation in PMN-PT single crystals is still not clear.

In this paper, the relationship between the domain structure and piezoelectric properties in a PMN-PT crystal with a MnO_x nanocomposite electrode was investigated. Two methods, electron beam lithography and focused ion-beam milling, are commonly used for fabricating nanoscaled patterned electrodes with specific structures [29–31]. Although a complicated patterned metal electrode with size in the nanoscale can be fabricated using these techniques, the throughput is relatively low and the process can be costly. In this work, MnO_x nanocomposite electrodes were fabricated using Lloyd's mirror interference lithography (LIL), a proved scalable nanofabrication technique [32,33]. After the heat treatment, Mn from the MnO_x nanocomposite was found to be diffused into PMN-PT crystals. ToF-SIMS was used to analyze the depth profile of diffused Mn. The influence of the nanocomposite on electric fields in PMN-PT single crystals was simulated using COMSOL. The dielectric and piezoelectric properties of the PMN-PT single crystals were measured using LCR meter and laser vibrometer system, respectively. To provide a better understanding of how the domain structure is modified by the patterned electrodes, samples with different thicknesses were studied using piezoresponse force microscopy (PFM). The mechanisms contributing to the enhanced property in the PMN-PT single crystals with nanocomposite electrodes will be elucidated using the combined ToF-SIMS, COMSOL simulation, and PFM results.

2. Experimental section

2.1. Fabrication of nanocomposite electrodes

For the nanocomposite electrode fabrication, LIL is an effective technique for fabricating nanograting structures, which allows for control of electrode structure sizes and features on large exposure areas [28]. The distance between the nanogratings could be controlled by using the interference equation:$\Lambda = \lambda/(2n \sin\theta)$, where Λ is the grating period, n is the refractive index ($n_{air} = 1$), λ is the wavelength of the ultraviolet laser (325 nm), and θ is the incident angle of light/laser. In this experiment, a precise pitch of 800 nm was obtained with a light incident angle of 11.7°. First, a 200 nm layer of photoresist (Sumitomo PFI-88A1/2) was coated on the [001]-grown PMN-PT single crystal (CTS Corporations, IL, USA). Then, the light intensity pattern was recorded by the photoresist to form a 1D grating nanostructure. The nanograting was fabricated parallel to $[010]_C$ direction, as shown in Fig. 1(a). After the photoresist exposure and development, a 100 nm thick Mn metal layer was deposited on the PMN-PT crystal with a nanostructured photoresist by electron-beam evaporation. The lift-off of Mn was implemented by using acetone. After the lift-off process, a Mn nanograting layer was left on the top surface of the PMN-PT crystal. After that, the sample was annealed at 800 °C for 3 h in air. During the high temperature (800 °C) treatment, the conducting Mn metal layer was oxidized forming a semiconducting MnO_x layer [18,34]. The surface morphology of the MnO_x nanograting is shown in Fig. 1(b). Lastly, a blanket layer of 5 nm thick Ti and 100 nm thick gold was deposited on the entire top surface of the sample as the conducting layer, as shown in Fig. 1(c). This nanocomposite electrode was then finally prepared including MnO_x semiconductor nanogratings with the pitch of 800 nm (MnO_x line width of 500 nm and spacing between two neighboring MnO_x lines of 300 nm) and a Ti/Au conductive layer (5/100 nm thick). The direction of nanocomposite electrode was along $[010]_C$.

2.2. PMN-PT sample preparation

After the nanocomposite electrode fabrication process, a [001]-grown PMN-PT single crystal wafer with dimension of 25 mm × 25 mm × 0.6 mm was diced into rectangular plates ($4 \times 4 \times 0.6$ mm^3) for experiments. Different thicknesses of samples were prepared by lapping and polishing from the bottom of samples. The root mean squared roughness (R_q) was well controlled below 5 nm, as measured by scanning probe microscopy (Dimension Icon, Bruker, Santa Barbara, CA). Ti/Au electrodes were deposited on the bottom surface of the PMN-PT samples to create the parallel-plate capacitors. Lastly, all samples were poled at an electric field amplitude of 10 kV/cm for 30 min at room temperature in air.

2.3. PFM measurements

The domain morphology of PMN-PT single crystals was characterized by a piezoresponse force microscopy, PFM (Dimension Icon, Bruker, Santa Barbara, CA). PFM is a versatile method for studying ferroelectric domain structure by applying an electrical voltage to the sample surface with a conductive tip of a scanning force microscope[18]. PFM requires detection of small tip displacements induced by inverse piezoelectric oscillations from the sample. A sample with rough surfaces could significantly affect the PFM image. Thus, careful lapping and polishing are needed to ensure the sample surface is smooth. The samples were waxed on the glass substrate and lapped down to certain thicknesses (200 μm, 50 μm,
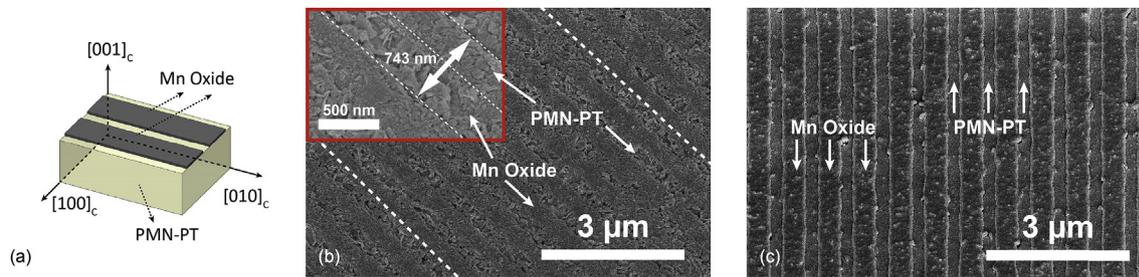
Fig. 1. The schematic and SEM image of fabrication results. (a) The MnO_x nanograting was fabricated parallel to $[010]_C$ direction (b) the MnO_x nanograting pattern on PMN-PT single crystal surface, (c) it shows the clear MnO_x nanocomposite electrodes after 100 nm gold electrode deposition.

and 30 μm). To avoid contacting and destroying the nanocomposite electrode, the lapping and polishing were done on the non-composite side (bottom side). Polishing was conducted right after the lapping process. The samples were polished with a 300 nm Al_2O_3 slurry (a mixture of deionized water and Al_2O_3 in volume rato of 6:1) and finally with a 50 nm Al_2O_3 slurry. After the polishing, the Rq of the samples were measured below 5 nm.

2.4. Time-of-flight secondary ion mass spectrometry (ToF-SIMS)

In ToF-SIMS measurements, a finely focused, pulsed primary ion beam is rastered across the sample surface and the secondary ions emitted to each pixel are extracted into a time of flight mass spectrometer, mass filtered, and then counted [35]. With dual beam operation, a depth profile of ions can be obtained, and a quantification of elements can be achieved that is standardized. ToF-SIMS analyses were conducted using a TOF-SIMS V (ION TOF, Inc. Chestnut Ridge, NY) instrument equipped with a Bi_n^{m+} (n = 1–5, m = 1, 2) liquid metal ion gun, Cs^+ sputtering gun. Both the Bi and Cs ion columns were oriented at 45° with respect to the sample surface normal. A pulsed Bi^{3+} primary ion beam at a 25 keV impact energy with less than a 1 ns pulse width was used. For depth profiles acquired in this study, 1 keV Cs ion with a 7.5 nA current was used to create a 120 μm by 120 μm area, and the middle 50 μm by 50 μm area was analyzed using a 0.3 pA Bi^{3+} primary ion beam. The sputtering time for with and without diffusion samples was 560 s and 335 s over the area, respectively.

2.5. Piezoelectric properties measurement

The dielectric properties were measured using a LCR meter (KEYSIGHT technologies, E4980A, Santa Clara, CA). To measure the piezoelectric coefficient of the PMN-PT single crystals, a d_{33} measurement setup that combined with a high-resolution (<10 p.m.) laser vibrometer (Polytec, OFV-5000, Irvine, CA) and a function generator (Tektronix, AFG3101, Lake Mary, FL) was used. The displacement of the sample was recorded by the laser vibrometer and an oscilloscope (Agilent Technologies Inc., DSO7104b, Santa Clara, CA).

3. Results and discussion

3.1. Simulation of the electric flux distribution

In domain engineering, nucleation of new domains is a critical step in the evolution of polarization reversal [15,36]. However, the mechanism of domain nucleation during application of electric fields is still not clear, because it is difficult to observe the appearance of an individual nanoscaled domain [20,37]. The key factors that may affect domain nucleation are the activation electric field for the domain nucleation, the averaged electric field over the volume of individual nuclei, the shape of the nuclei, and temperature [15]. Previous experimental studies of a $LiNbO_3$ single crystal with a micron-scaled stripe-patterned electrode revealed that most of the domain nucleation sites occur near the edge of the electrodes, and that this enhancement of domain nucleation result from the spatial electric field distribution [20,38]. The stripe-patterned electrodes had a 2.6 μm periodicity on the surface of the $LiNbO_3$ ceramic and resulted in the nucleation of needle-like domains [11].

Yamashita et al. reported a PMN-PT crystal with random-patterned MnO_x composite electrodes could exhibit a ~40% enhancement in the dielectric and piezoelectric constants [18]. The random-patterned MnO_x composite electrodes did change the piezoelectric properties. However, the mechanisms of the pattern effects were not mentioned in the report. In our previous study, uneven electric fields were found beneath the nanocomposite electrodes [28]. In the present work, the nanocomposite electrodes consist of a periodical MnO_x semiconductor nanograting and a coating with a Ti/Au conductive layer. The nanocomposite electrodes could screen part of the electric field based on different materials. To have a better understanding of the influence of nanocomposite electrodes on the local electric fields in the sample, COMSOL was used to simulate the electrical flux distribution in PMN-PT crystals with a patterned electrode. The width and thickness of the MnO_x nanograting used for simulation were 500 nm and 100 nm, respectively. The spacing between MnO_x nanogratings was 300 nm. Thus, the pitch size of the MnO_x nanograting on the surface of PMN-PT crystal was 800 nm. A ground boundary condition
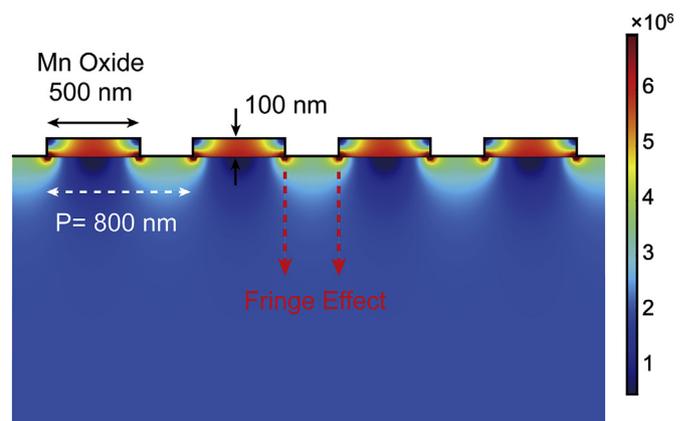
Fig. 2. The fringe effect simulation of MnO_x nanocomposite electrode. The MnO_x nanograting has an 800 nm period with pattern size 500 nm and 100 nm in width and thickness, respectively. The color bar denotes the electric field intensity. (For interpretation of the references to colour in this figure legend, the reader is referred to the web version of this article.)

was assigned to the bottom electrode, and 100 V was applied across a 600 μm thick PMN-PT crystal. Fig. 2 shows the simulated electric flux distribution in the PMN-PT crystal. On the edge of each MnO_x nanograting, a strongly non-uniform electric field was generated by a fringe effect. Beneath the edge of the MnO_x nanograting, the electric field was found to be three to six times higher than the area between the two nanogratings or at the center area of the nanograting. Consequently, a larger quantity of the new domains was formed at the edge of the MnO_x nanograting, since the region had a higher electric field that could easily exceed the activation field of domain nucleation. The needle-like domains propagated, forming nuclei that were parallel to the direction of applied field [15]. The non-uniform electric fields created by the nanocomposite electrodes on the PMN-PT crystal may lead to a higher domain density at the edge of the MnO_x nanograting, as well as prevent rapid domain reversal during application of electric field [18]. The difference in domain reversal timing may produce larger charged domain boundary regions and dense domains of the PMN–PT single crystal. Thus, the simulation result illustrates the electric field spatial distribution and the favored regions for domain nucleation. The fringe effect observed in the simulation result is similar with the work reported by Shur et al. [20].

3.2. Mn doping/diffusion analysis

Heat treatment of the PMN-PT crystals during the nanocomposite electrode fabrication process may result in the doping/diffusion of Mn ions into PMN-PT. In order to maintain charge neutrality, it is known that the formation of oxygen vacancies is needed when acceptor dopants (Mn^{2+}) substitute onto the B-site (e.g., Ti^{4+}, Mg^{3+}, and Nb^{5+}) in PMN-PT [39]. The oxygen vacancies tend to diffuse along the direction opposite to that of the orientation of polarization, forming a defect dipole [40]. These oxygen vacancies may promote the domain nucleation rate in PMN-PT crystals with MnO_x nanocomposite electrodes. ToF-SIMS was employed to quantify the diffusion of Mn ions. Two PMN-PT crystals with Mn oxide nanogratings, with and without heat treatment, were prepared for the ToF-SIMS analysis and the results are shown in Fig. 3. There are three regions in each figure; they are a MnO_x region, an interface region and a PMN-PT single crystal region (from left to right). The material was sputtered using a Cs ion beam from the top surface of the nanocomposite which is the MnO_x layer. Atomic force microscopy with a tapping mode was used to measure the crater depth in the bombarded area, and the measured crater depth was used to calculate the sputtering rate. As the material was progressively removed, the intensity of Mn ion decreased, and the intensities of Ti and Pb ions increased, commensurate with the

location of the interface region. The intensity of Mn ion reached a plateau in the PMN-PT single crystal region as the top nanocomposite electrode and interfaces were being completely removed by the ion beam. The sample without heat treatment shows the Mn ion intensity starts to drop significantly at a depth of ~80 nm (in the interface region) and reaches a minimum at a depth of ~130 nm, as shown in Fig. 3(a). Below this depth (the red region of the figure), the intensity of Ti and Pb ions were stable, which means that the sputtered materials mostly come from PMN-PT. On the other hand, a significant doping/diffusion of Mn into PMN-PT was found in the sample that was heat treated, as shown in Fig. 3(b). The intensity of the Mn ion curve evidenced that the depth of Mn doping/diffusion was ~300 nm.

3.3. Domain structure analysis

In order to understand the influence of nanocomposite electrodes on the domain structure, domain morphologies of the PMN-PT crystals with different thicknesses were acquired using PFM. The high spatial resolution of PFM makes it ideal for the study of domain morphology changes on the nanometer scale [41]. In a control group, the domain structure of 30 μm and 200 μm thick crystals with planar electrodes were measured by PFM. The out-of-plane polarization phase images are shown in Fig. 4(a) and (b), and their topography images are shown in the insets. The surface roughnesses (root mean square) were less than 5 nm. The PFM images revealed that both samples (of different thickness) with planar electrodes had a randomly distributed ribbon-shaped domain structure as previously reported by Shvartsman et al. [42].

The PFM images of PMN-PT crystals (thicknesses of 30, 200 and 600 μm) with nanocomposite electrodes are shown in Fig. 5. The PFM image of the 600 μm thick crystal had a similar ribbon-shaped domain structure to the crystal with a planar electrode (see Fig. 4(a) and (b)). When the sample thickness was decreased to 200 μm, linear domain structures which were parallel to the direction of the MnO_x nanogratings, $[010]_C$ direction, were observed. Similar linear domain structures were also observed in the 30 μm thick crystal. The linear domain structure may be induced by the fringe effect at the edges of nanocomposite electrode. The fringe effect provides a high electric field gradient locally, which may favor nuclei formation. Thus, more domains may be nucleated along the edge of the MnO_x nanograting, resulting in the linear domain structures. The nucleation probability (P) is proportional to $\exp\left(\frac{-E_{active}}{E_{local}}\right)$, where E_{active} is the activation field and E_{local} is the electric field averaged over the volume of the nucleus [20]. When the thickness of the crystal is above a critical value, the polar nuclei forming near the
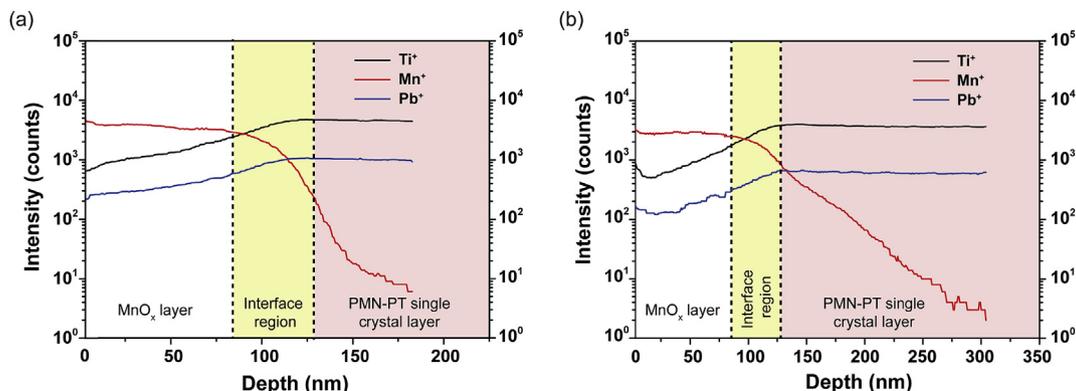
Fig. 3. ToF-SIMS results of MnO_x nanocomposite electrodes with and without heat treatment (a) PMN-PT without heat treatment; (b) PMN-PT after heat treatment.
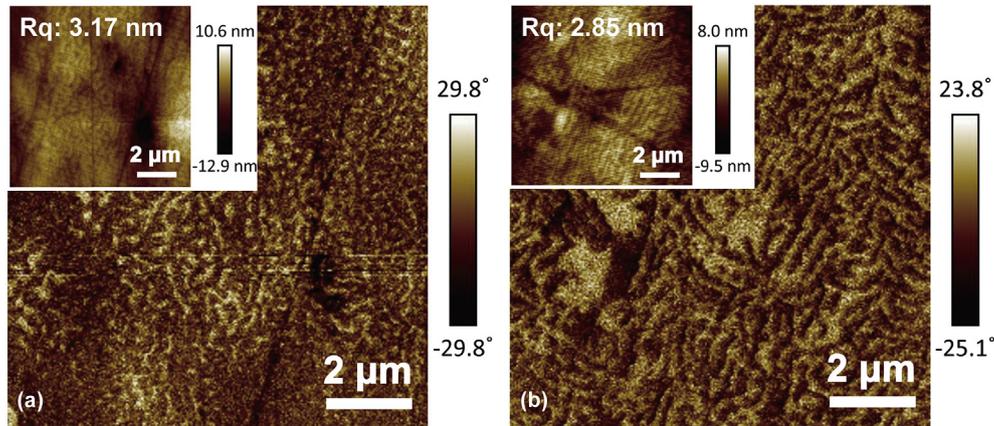
Fig. 4. The PFM domain image of PMN-PT with conventional planar electrodes in different thicknesses. (a) The thickness of the sample is 30 μm, and (b) 200 μm; the insert images are the topography and surface roughness.
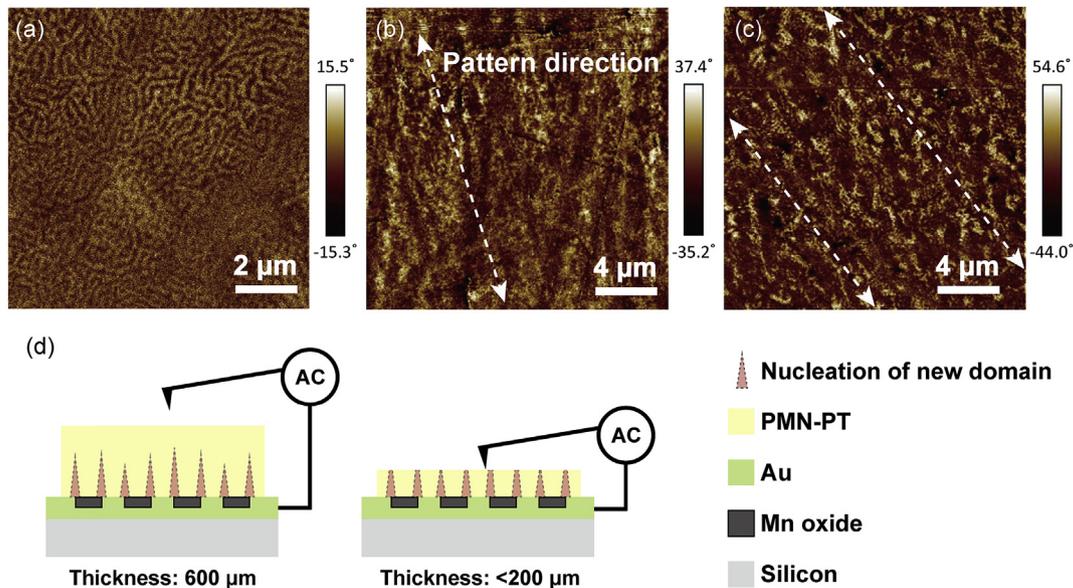
Fig. 5. The PFM domain image result of PMN-PT with MnO$_x$ nanocomposite electrodes in different thicknesses. (a) 600 μm (b) 200 μm (c) 30 μm (d) schematic images of nucleation of new domain observation by PFM for samples in different thickness.

nanocomposite electrodes do not grow throughout the crystal volume. Part of the new-forming domains merge together in the crystal, resulting in a randomly oriented ribbon-shaped domain morphology (see Fig. 5(a)). However, as the sample thickness is reduced, the fringe effect can only influence the process up to a depth of 200 μm, resulting in a linear domain morphology (See Fig. 5(b) and (c)). A schematic of the domain growth process in crystals with different thickness is given in Fig. 5(d), summarizing our plausible explanation for why the nanocomposite electrode can generate two different types of domain distributions in crystals of different thicknesses. Similar linear domain patterns were also found in a 50 μm thick PMN-PT crystal, as shown in Fig. 6(a) and (b). The zoomed-in PFM image (Fig. 6(c)) shows the linear domain pattern had a width of 150 nm. This figure also demonstrates near-periodic linear domain structures with a periodicity of ~300 nm. Fig. 6(d) shows the phase intensity, which is illustrated as a dash-line in Fig. 6(c). Changes in the phase signal intensity matched well with the MnO$_x$ nanocomposite electrode pattern. Furthermore, the MnO$_x$ nanocomposite electrode on the 50 μm thick PMN-

PT crystal clearly generated a periodic linear domain pattern over the entire sample surface.

Based on these experimental observations, a MnO$_x$ nanocomposite electrode can be used to generate different nanodomain patterns in PMN-PT single crystals. A patterned domain structure with a high domain density could be generated by a combination of the fringe effect and the diffusion of Mn. When the domain density increased, the piezoelectric properties have shown significant enhancement [43].

3.4. Ferroelectric hysteresis measurements

Fig. 7 shows the polarization-electric field loops (*P-E* loop) of PMN-PT crystals with and without nanocomposite electrodes. The samples were treated with the same poling condition. The 600 μm thick PMN-PT crystals with and without nanocomposite electrodes exhibited similar and well-saturated *P-E* loops under application of a triangular bipolar waveform (f = 1 Hz) with an amplitude of 10 kV/cm. Before each measurement of hysteresis loop, a preset
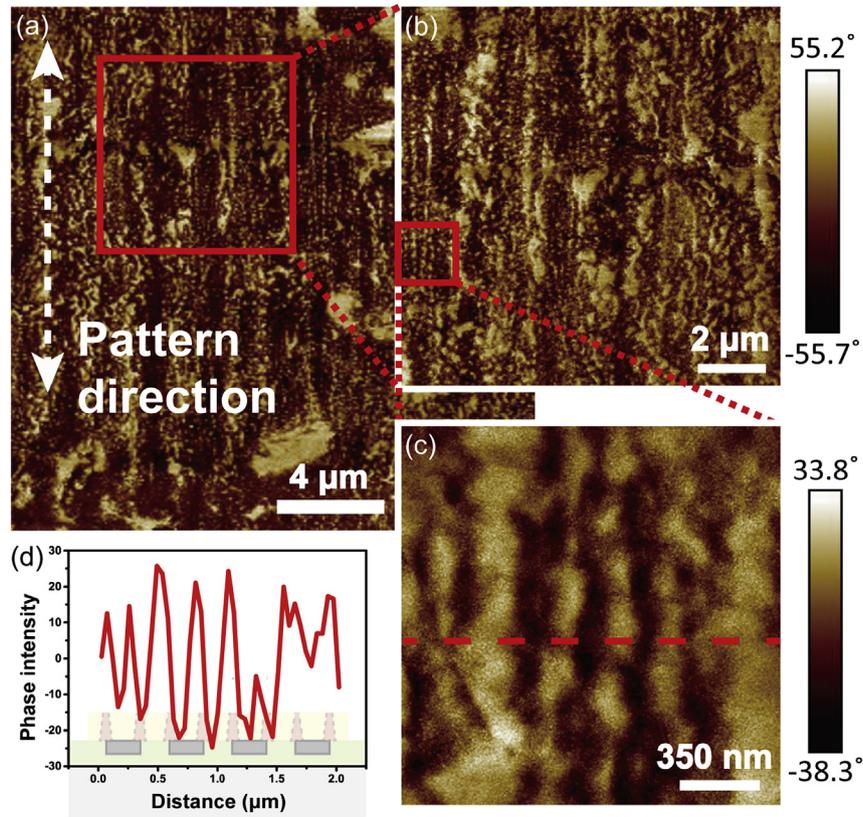
Fig. 6. PFM images of MnO$_x$ nanocomposite electrodes PMN-PT single crystal with 50 μm thickness. (a) The domain pattern along the edge of original grating electrode with 20 × 20 μm^2 scanning area; (b) and (c) are the enlarge figures with 10 × 10 and 2 × 2 μm^2 scanning area; (d) the phase diagram of the cross section in (c), and the waviness phase signal follow the edge of MnO$_x$, positive and negative phases indicate different domains.
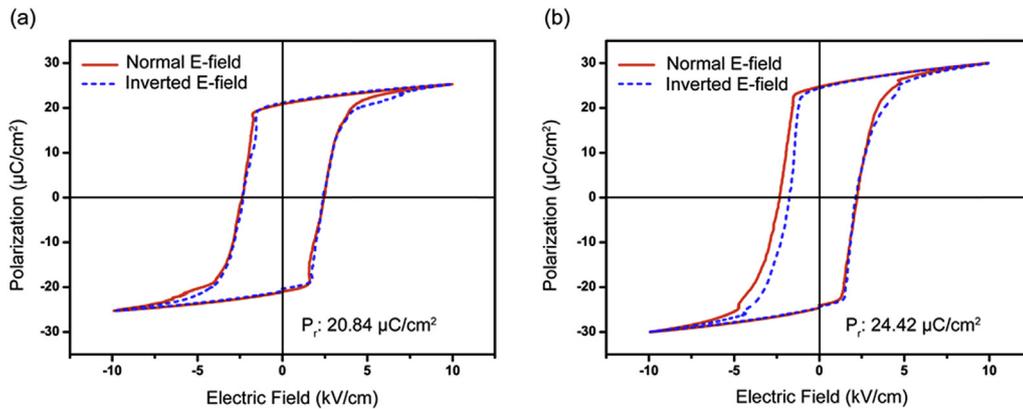
Fig. 7. Normal and inverted electric field (E-field) induced ferroelectric (P—E) hysteresis loop. (a) PMN-PT with conventional planar electrodes. (b) PMN-PT with nanocomposite electrodes on one surface and a plane electrode on the other surface.

pulse E-field (10 kV/cm) is applied on the sample. The hysteresis loop was recorded after 20 loop cycles. PE curves of each sample were collected under two different electric field conditions, which we designate here as normal and inverted electric fields. The normal electric field is along the direction from the nano-electrodes to the opposite surface, and the inverted field is reversed. Fig. 7(a) shows the P-E loops for a sample without a nanocomposite electrode under both normal and inverted electric fields. Similar P-E loops with a remnant polarization (P_r) of 20.48 μC/cm^2 and a coercive electric field (E_c) of 2.45 kV/cm were observed in both cases. On the other hand, the P-E loops of PMN-PT with nanocomposite

electrodes are shown in Fig. 7(b). The values of P_r and E_c were 24.42 μC/cm^2 and 2.24 kV/cm, respectively. Under the normal electric field, the Mn nanograting induced oxygen vacancy was accumulated on the surface and formed a lower internal bias field, $E_i = 0.05$ kV/cm. Under the inverted electric field, the oxygen vacancy migrated to the whole crystal and formed a higher internal bias field, $E_i = 0.18$ kV/cm. Compared to the sample without nanocomposite electrodes, the P-E loops of samples with the nanocomposite electrodes were slim (decrease 5.7%) and non-symmetric (internal bias field $E_i = 0.18$ kV/cm). Also, the E_c of normal and inverted electric fields were clearly not equal. The
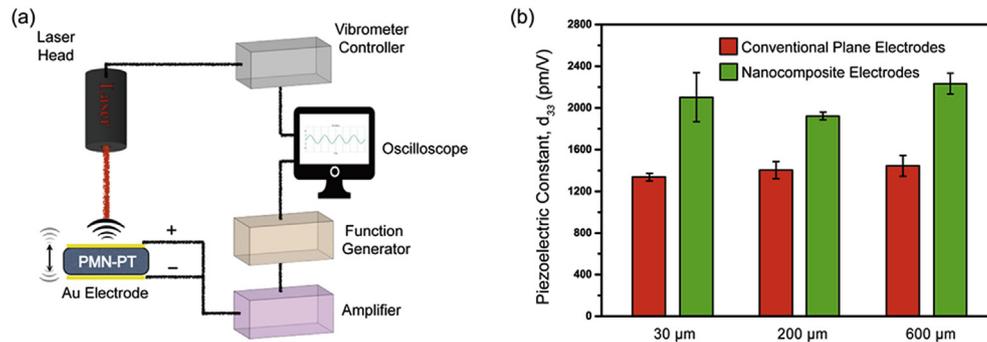
Fig. 8. Piezoelectric coefficient measurement system and results. (a) The piezoelectric coefficient measurement system which including a laser vibrometer system, a function generator, an amplifier and an oscilloscope. (b) The piezoelectric constant of PMN-PT with MnO_x nanocomposite electrodes and conventional planar electrodes in three different thicknesses, 30 μm, 200 μm and 600 μm. The standard deviation (error bar) of piezoelectric constant for plane electrode sample 20 μm, 200 μm and 600 μm were 37 pC/N, 82 pC/N, and 100 pC/N respectively. The standard deviation of piezoelectric constant for structured electrode sample 20 μm, 200 μm and 600 μm were 234 pC/N, 37 pC/N, and 150 pC/N respectively.

slimmer loop demonstrates reduced hysteretic losses under high amplitude drive. The non-symmetric nature results in a horizontal shift in the P-E loops, indicating the presence of internal dipolar fields that bias the crystal [44]. The inverted electric field hysteresis data for PMN-PT with nanocomposite electrodes showed a partially poled phenomenon. The PMN-PT samples with nanocomposite electrodes were partially poled during the P-E measurement with lower field amplitudes. This dipolar field from the Mn doping might be leading to the asymmetry offset in the P-E loops.

3.5. Piezoelectric constant measurements

The illustration of the setup is shown in Fig. 8(a). A sine wave with an electric field amplitude of 1.6 kV/cm was applied to the crystal at a frequency of 1 Hz. The piezoelectric coefficient (d_{33}) was then calculated by dividing the measured displacement by the applied voltage. PMN-PT crystals with three different thicknesses (30 μm, 200 μm, and 600 μm) and different electrodes (nanocomposite electrodes and conventional planar electrodes) were studied. To minimize the compositional differences between the samples, the samples used in this work were prepared from the same section of the PMN-PT crystal. The thickness variation will cause the measuring error of the piezoelectric constant. The thickness of samples was measured by using length gauge (CT 6000, Heidenhain, Traunreut, Germany) three times for each sample and the error of thickness measuring was less than 1%. Before measuring d_{33}, the samples were put away for 24 h after poling to reach a stable state. For each condition, three samples were prepared. And the d_{33} were measured at three different locations of each sample. The data shown in Fig. 8 (b) is the statistical average d_{33} and the measuring error was less than 3%. The d_{33} value of PMN-PT crystal with the plane electrode is consistency with Tian's works [45] and Zhang's works [46] around 1600 pC/N. PMN-PT samples with nanocomposite electrodes showed a higher d_{33} value of 2050 ± 150 p.m./V than the ones with planar electrodes. Three samples with same conditions were prepared, and the data were averaged from three samples with three different locations. The standard deviation of the piezoelectric constant for plane electrode sample 20 μm, 200 μm and 600 μm were 37 pC/N, 82 pC/N, and 100 pC/N respectively. The standard deviation of the piezoelectric constant for structured electrode sample 20 μm, 200 μm and 600 μm were 234 pC/N, 37 pC/N, and 150 pC/N respectively. The dielectric constant was measured by a LCR meter. PMN-PT samples with nanocomposite electrodes showed a dielectric constant value of 5400, and the ones with planar electrodes were 3905. The values of the dielectric and piezoelectric

constants of the PMN-PT crystal with the nanocomposite electrodes were 38.3% and 36.7% higher than the crystal with a conventional planar electrode, respectively. The d_{33} value of the crystal with conventional electrodes did have a modest increase of about 8% as the thickness was increased from 30 μm to 600 μm because of the clamping/pinning of domain wall motion was reduced in the thicker samples [47]. These improvements could be explained directly due to the patterned electrodes.

4. Conclusion

Single crystals of PMN-PT with MnO_x nanocomposite electrodes showed a high d_{33} value and dielectric constant, which were 36.7% and 38.3% higher than the ones with a conventional planar gold electrode, respectively. The enhanced d_{33} may be due to the higher domain densities which originate from two domain nucleation mechanisms: Mn doping/diffusion and the fringe effect. ToF-SIMS investigations demonstrated that the doping/diffusion of the Mn into PMN-PT may result in defect dipoles, which resulted in a slightly asymmetric characteristic in the P-E loops. PFM images revealed an increase in the domain density for crystals with nanocomposite electrodes when the crystal thickness was less than 200 μm. The simulation results show a fringe effect beneath the edge of the patterned MnO_x nanograting. The non-uniform electric fields resulting from the MnO_x nanocomposite electrode in the PMN-PT may increase the domain nucleation rate and prevent rapid domain reversal. Thus, nucleation of small domains with reversed polarization will occur first in local regions that have higher electric fields. This work provides a better understanding of PMN-PT single crystals with tailored MnO_x nanocomposite electrodes for improving piezoelectric properties.

References

[1] T.R. Shrout, Z.P. Chang, N. Kim, S. Markgraf, Dielectric behavior of single

crystals near the (1—X) Pb(Mg1/3Nb2/3)O3-(x) PbTiO3 morphotropic phase boundary, Ferroelectr. Lett. Sect. 12 (1990) 63—69, https://doi.org/10.1080/07315179008201118.

[2] X. Zhao, B. Fang, H. Cao, Y. Guo, H. Luo, Dielectric and piezoelectric performance of PMN—PT single crystals with compositions around the MPB: influence of composition, poling field and crystal orientation, Mater. Sci. Eng. B 96 (2002) 254—262, https://doi.org/10.1016/S0921-5107(02)00354-9.

[3] Z.-G. Ye, M. Dong, Morphotropic domain structures and phase transitions in relaxor-based piezo-/ferroelectric (1—x)Pb(Mg1/3Nb2/3)O3—xPbTiO3 single crystals, J. Appl. Phys. 87 (2000) 2312—2319, https://doi.org/10.1063/1.372180.

[4] Z.-G. Ye, B. Noheda, M. Dong, D. Cox, G. Shirane, Monoclinic phase in the relaxor-based piezoelectric/ferroelectric Pb(Mg1/3Nb2/3)O3— PbTiO3 system, Phys. Rev. B 64 (2001) 184114, https://doi.org/10.1103/PhysRevB.64.184114.

[5] S. Zhang, F. Li, High performance ferroelectric relaxor-PbTiO3 single crystals: status and perspective, J. Appl. Phys. 111 (2012) 031301, https://doi.org/10.1063/1.3679521.

[6] S. Choudhury, Y. Li, L.-Q. Chen, A phase diagram for epitaxial PbZr1—xTiO3 thin films at the bulk morphotropic boundary composition, J. Am. Ceram. Soc. 88 (2005) 1669—1672, https://doi.org/10.1111/j.1551-2916.2005.00319.x.

[7] Q.M. Zhang, H. Wang, N. Kim, L.E. Cross, Direct evaluation of domain-wall and intrinsic contributions to the dielectric and piezoelectric response and their temperature dependence on lead zirconate-titanate ceramics, J. Appl. Phys. 75 (1994) 454—459, https://doi.org/10.1063/1.355874.

[8] S. Wada, S.-E. Park, L.E. Cross, T.R. Shrout, Engineered domain configuration in rhombohedral PZN-PT single crystals and their ferroelectric related properties, Ferroelectrics 221 (1999) 147—155, https://doi.org/10.1080/00150199908016449.

[9] M. Davis, D. Damjanovic, D. Hayem, N. Setter, Domain engineering of the transverse piezoelectric coefficient in perovskite ferroelectrics, J. Appl. Phys. 98 (2005) 014102, https://doi.org/10.1063/1.1929091.

[10] S. Zhang, T.R. Shrout, Relaxor-PT single crystals: observations and developments, IEEE Trans. Ultrason. Ferroelectr. Freq. Control 57 (2010) 2138—2146, https://doi.org/10.1109/TUFFC.2010.1670.

[11] V.Y. Shur, E.L. Rumyantsev, E.V. Nikolaeva, E.I. Shishkin, D.V. Fursov, R.G. Batchko, L.A. Eyres, M.M. Fejer, R.L. Byer, J. Sindel, Formation of self-organized nanodomain patterns during spontaneous backswitching in lithium niobate, Ferroelectrics 253 (2001) 105—114, https://doi.org/10.1080/00150190108008448.

[12] Z.-G. Ye, Handbook of Advanced Dielectric, Piezoelectric and Ferroelectric Materials: Synthesis, Properties and Applications, Elsevier, 2008.

[13] R.G. Batchko, V.Y. Shur, M.M. Fejer, R.L. Byer, Backswitch poling in lithium niobate for high-fidelity domain patterning and efficient blue light generation, Appl. Phys. Lett. 75 (1999) 1673—1675.

[14] S. Wada, K. Yako, H. Kakemoto, T. Tsurumi, T. Kiguchi, Enhanced piezoelectric properties of barium titanate single crystals with different engineered-domain sizes, J. Appl. Phys. 98 (2005) 014109, https://doi.org/10.1063/1.1957130.

[15] V. Shur, E. Rumyantsev, R. Batchko, G. Miller, M. Fejer, R. Byer, Physical basis of the domain engineering in the bulk ferroelectrics, Ferroelectrics 221 (1999) 157—167, https://doi.org/10.1080/00150199908016450.

[16] S. Wada, K. Yako, T. Muraishi, K. Yokoh, S.-M. Nam, H. Kakemoto, T. Tsurumi, Enhanced piezoelectric property of barium titanate single crystals by domain wall engineering using patterning electrode, Ferroelectrics 340 (2006) 17—24, https://doi.org/10.1080/00150190600888652.

[17] S.H. Baek, J. Park, D.M. Kim, V.A. Aksyuk, R.R. Das, S.D. Bu, D.A. Felker, J. Lettieri, V. Vaithyanathan, S.S.N. Bharadwaja, N. Bassiri-Gharb, Y.B. Chen, H.P. Sun, C.M. Folkman, H.W. Jang, D.J. Kreft, S.K. Streiffer, R. Ramesh, X.Q. Pan, S. Trolier-McKinstry, D.G. Schlom, M.S. Rzchowski, R.H. Blick, C.B. Eom, Giant piezoelectricity on Si for hyperactive MEMS, Science 334 (2011) 958—961, https://doi.org/10.1126/science.1207186.

[18] Y. Yohachi, J. John, N. Yamamoto, K. Itsumi, Y. Hosono, Effects of manganese oxides/gold composite electrode on piezoelectric properties of lead magnesium niobate titanate single crystal, Jpn. J. Appl. Phys. 50 (2011) 09NC05, https://doi.org/10.1143/JJAP.50.09NC05.

[19] J. Pattanayak, V.S. Rao, H.S. Maiti, Electrical resistivity measurements on the Mn2O3-Mn3O4 phase transformation, J. Mater. Sci. Lett. 8 (1989) 1405—1407, https://doi.org/10.1007/BF00720203.

[20] V.Y. Shur, Kinetics of Ferroelectric Domains: Application of General Approach to LiNbO3 and LiTaO3, in: Front. Ferroelectr., Springer, US, 2006, pp. 199—210, https://doi.org/10.1007/978-0-387-38039-1_18.

[21] R. Landauer, Electrostatic considerations in BaTiO3 domain formation during polarization reversal, J. Appl. Phys. 28 (1957) 227—234, https://doi.org/10.1063/1.1722712.

[22] Y. Xiang, R. Zhang, W. Cao, Optimization of piezoelectric properties for [001]c poled 0.94Pb(Zn1/3Nb2/3)O3—0.06PbTiO3 single crystals, Appl. Phys. Lett. 96 (2010), https://doi.org/10.1063/1.3314285.

[23] G. Rosenman, K. Garb, A. Skliar, Domain broadening in quasi-phase-matched nonlinear optical devices, Appl. Phys. Lett. 73 (1998) 865—867, https://doi.org/10.1063/1.121969.

[24] L.-H. Peng, Y.-P. Tseng, K.-L. Lin, Z.-X. Huang, C.-T. Huang, A.-H. Kung, Depolarization field mitigated domain engineering in nickel diffused lithium

tentalate, Appl. Phys. Lett. 92 (2008) 092903, https://doi.org/10.1063/1.2890728.

[25] P. Gao, C.T. Nelson, J.R. Jokisaari, S.-H. Baek, C.W. Bark, Y. Zhang, E. Wang, D.G. Schlom, C.-B. Eom, X. Pan, Revealing the role of defects in ferroelectric switching with atomic resolution, Nat. Commun. 2 (2011) 591, https://doi.org/10.1038/ncomms1600.

[26] G. Holzlechner, M. Kubicek, H. Hutter, J. Fleig, A novel ToF-SIMS operation mode for improved accuracy and lateral resolution of oxygen isotope measurements on oxides, J. Anal. At. Spectrom. 28 (2013) 1080—1089, https://doi.org/10.1039/C3JA50059D.

[27] G. Holzlechner, D. Kastner, C. Slouka, H. Hutter, J. Fleig, Oxygen vacancy redistribution in PbZrxTi1—xO3 (PZT) under the influence of an electric field, Solid State Ion. 262 (2014) 625—629, https://doi.org/10.1016/j.ssi.2013.08.027.

[28] W.-Y. Chang, W. Huang, A. Bagal, C.-H. Chang, J. Tian, P. Han, X. Jiang, Study on dielectric and piezoelectric properties of 0.7 Pb(Mg1/3Nb2/3)O3-0.3 PbTiO3 single crystal with nano-patterned composite electrode, J. Appl. Phys. 114 (2013) 114103, https://doi.org/10.1063/1.4821517.

[29] S. Bühlmann, B. Dwir, J. Baborowski, P. Muralt, Size effect in mesoscopic epitaxial ferroelectric structures: increase of piezoelectric response with decreasing feature size, Appl. Phys. Lett. 80 (2002) 3195—3197, https://doi.org/10.1063/1.1475369.

[30] S. Bühlmann, P. Muralt, S.V. Allmen, Lithography-modulated self-assembly of small ferroelectric Pb(Zr,Ti)O3 single crystals, Appl. Phys. Lett. 84 (2004) 2614—2616, https://doi.org/10.1063/1.1690873.

[31] P. Muralt, Recent progress in materials issues for piezoelectric MEMS, J. Am. Ceram. Soc. 91 (2008) 1385—1396, https://doi.org/10.1111/j.1551-2916.2008.02421.x.

[32] K.-C. Park, H.J. Choi, C.-H. Chang, R.E. Cohen, G.H. McKinley, G. Barbastathis, Nanotextured silica surfaces with robust superhydrophobicity and omnidirectional broadband supertransmissivity, ACS Nano 6 (2012) 3789—3799, https://doi.org/10.1021/nn301112t.

[33] A. Bagal, E.C. Dandley, J. Zhao, X.A. Zhang, C.J. Oldham, G.N. Parsons, C.-H. Chang, Multifunctional nano-accordion structures for stretchable transparent conductors, Mater. Horiz. 2 (2015) 486—494, https://doi.org/10.1039/C5MH00070J.

[34] V. Berbenni, A. Marini, Oxidation behaviour of mechanically activated Mn3O4 by TGA/DSC/XRPD, Mater. Res. Bull. 38 (2003) 1859—1866, https://doi.org/10.1016/j.materresbull.2003.07.008.

[35] A.M. Belu, D.J. Graham, D.G. Castner, Time-of-flight secondary ion mass spectrometry: techniques and applications for the characterization of biomaterial surfaces, Biomaterials 24 (2003) 3635—3653, https://doi.org/10.1016/S0142-9612(03)00159-5.

[36] V.Y. Shur, Domain engineering in lithium niobate and lithium tantalate: domain wall motion, Ferroelectrics 340 (2006) 3—16, https://doi.org/10.1080/00150190600888603.

[37] V.Y. Shur, Fast polarization reversal process: evolution of ferroelectric domain structure in thin films, in: Ferroelectr. Thin Films Synth. Basic Prop, Taylor & Francis, US, 1996, p. 590.

[38] C.P. de Araujo, Ferroelectric Thin Films: Synthesis and Basic Properties, Taylor & Francis, US, 1996.

[39] G.A. Samara, The relaxational properties of compositionally disordered ABO3 perovskites, J. Phys. Condens. Matter. 15 (2003), R367, https://doi.org/10.1088/0953-8984/15/9/202.

[40] N. Luo, S. Zhang, Q. Li, Q. Yan, Y. Zhang, T. Ansell, J. Luo, T.R. Shrout, Crystallographic dependence of internal bias in domain engineered Mn-doped relaxor-PbTiO 3 single crystals, J. Mater. Chem. C 4 (2016) 4568—4576, https://doi.org/10.1039/C6TC00875E.

[41] S.V. Kalinin, A.N. Morozovska, L.Q. Chen, B.J. Rodriguez, Local polarization dynamics in ferroelectric materials, Rep. Prog. Phys. 73 (2010) 056502, https://doi.org/10.1088/0034-4885/73/5/056502.

[42] V.V. Shvartsman, A.L. Kholkin, Domain structure of 0.8 Pb(Mg1/3Nb2/3)O3—0.2 PbTiO3 studied by piezoresponse force microscopy, Phys. Rev. B 69 (2004) 014102, https://doi.org/10.1103/PhysRevB.69.014102.

[43] Y.U. Wang, Field-induced inter-ferroelectric phase transformations and domain mechanisms in high-strain piezoelectric materials: insights from phase field modeling and simulation, J. Mater. Sci. 44 (2009) 5225—5234, https://doi.org/10.1007/s10853-009-3663-9.

[44] N. Balke, T. Granzow, J. Rödel, Degradation of lead-zirconate-titanate ceramics under different dc loads, J. Appl. Phys. 105 (2009) 104105, https://doi.org/10.1063/1.3126707.

[45] J. Tian, P. Han, D.A. Payne, Measurements along the growth direction of PMN-PT crystals: dielectric, piezoelectric, and elastic properties, IEEE Trans. Ultrason. Ferroelectr. Freq. Control 54 (2007) 1895—1902, https://doi.org/10.1109/TUFFC.2007.474.

[46] S. Zhang, C.A. Randall, T.R. Shrout, High Curie temperature piezocrystals in the BiScO3-PbTiO3 perovskite system, Appl. Phys. Lett. 83 (2003) 3150—3152, https://doi.org/10.1063/1.1619207.

[47] H.J. Lee, S. Zhang, J. Luo, F. Li, T.R. Shrout, Thickness dependent properties of relaxor-PbTiO3 ferroelectrics for ultrasonic transducers, Adv. Funct. Mater. 20 (2010) 3154—3162, https://doi.org/10.1002/adfm.201000390.